Available online at www.sciencedirect.com
SCIENCE DIRECT®
ELSEVIER
International Journal of Solids and Structures 41 (2004) 6249–6271
INTERNATIONAL JOURNAL OF SOLIDS and STRUCTURES
www.elsevier.com/locate/ijsolstr

A protocol for characterizing the structural performance of metallic sandwich panels: application to pyramidal truss cores

F.W. Zok *, S.A. Waltner, Z. Wei, H.J. Rathbun, R.M. McMeeking, A.G. Evans

Materials Department, University of California, Santa Barbara, CA 93106-5050, USA

Received 13 January 2004; received in revised form 19 May 2004
Available online 2 July 2004

Abstract

All-metallic sandwich panels with truss and prismatic cores have impending application as ultra-light load bearing panels amenable to simultaneous active cooling and blast resistance. To facilitate application, a protocol for characterizing the structural performance of such panels is needed that can be used for design calculations. An approach capable of realizing this objective is presented and demonstrated for panels with pyramidal truss cores. It combines measurements, mechanism maps, finite element simulations and optimization. Mechanism maps based on beam theory are used to characterize face and core dimensions as well as to estimate minimum weight designs. Experimental measurements and finite element calculations are used to calibrate and understand the responses of the core in transverse compression, in-plane shear and stretch. Overlaying the measurements and simulations allows assessment of the mechanical properties of the core material, as affected by fabrication. The updated results are used to establish and calibrate an orthotropic constitutive law for the core. Bending tests performed on panels subject to two end constraints are used to assess the fidelity of the core constitutive law. The tests are simulated by using a stress/strain response for the faces obtained from independent tensile measurements. The comparison reveals that the loads are predicted quite accurately. However, when controlled by the core, the simulations predict a more abrupt yield point than that found experimentally.

Keywords: Finite element model; Sandwich panel; Pyramidal core; Constitutive law; Clamped bending; Three-point bending

1. Introduction

Metallic sandwich panels with various truss, prismatic and textile cores have been devised, analyzed and tested (Ashby et al., 2000; Rathbun et al., 2004; Budiansky, 1999; Wicks and Hutchinson, 2001; Zok et al., 2003; Evans et al., 2001; Evans, 2001). Their lightweight attributes have been revealed, as well as their

* Corresponding author. Tel.: +1-805-8938699; fax: +1-805-8938486.
E-mail address: zok@engineering.ucsb.edu (F.W. Zok).

0020-7683/$ - see front matter © 2004 Elsevier Ltd. All rights reserved.
doi:10.1016/j.ijsolstr.2004.05.045

Nomenclature

B	beam width
d_c	face separation
E	Young's modulus
F	load
G	shear modulus
H	hardening modulus
H_c	core height
H_{eq}	equivalent thickness
k	buckling constant ($k = 1$ for pinned ends, 4 for built-in ends)
L_c	truss member length
M	moment per unit width
s	attachment length
S	span length
t_c	truss core member thickness
t_f	face sheet thickness
V	shear force per unit width
W	weight per unit area
α_{ij}	coefficients in core constitutive law
β	non-dimensional stretch resistance
δ	displacement
Δ	normalized displacement
δ_p	plastic displacement
ε_y	yield strain
ε_{pl}	plastic strain
ℓ	characteristic length scale ($\equiv M/V$)
Ψ	non-dimensional weight index
μ	friction coefficient
Π_b	load index
θ	angle between core member and face sheet
ρ	density of solid material
$\bar{\rho}_c$	relative core density ($\equiv \rho_c/\rho$)
ρ_c	density of core
σ_e	effective stress
σ_f	flow stress
σ_o	uniaxial yield strength of core
$\bar{\sigma}_{panel}$	panel tensile strength
σ_y	0.2% offset yield strength of solid
Σ	normalized load

potential for multifunctionality, and their ability to resist blast. The interest in such panels has been heightened by recent innovations in manufacturing. To establish the performance spectrum for panels of this type, a protocol for manufacturing, testing, analyzing and simulating their behavior must be devised. Such a protocol is envisioned to have three basic steps.

(i) *Sandwich panel design:* The core geometry is combined with beam theory analysis to characterize the *onset* of failure in bending and to define a failure map. On this basis, optimizations are performed to identify minimum weight designs. Panels with near-optimal configurations are then manufactured.

(ii) *Core characterization:* The core response is measured in transverse compression, shear and in-plane tension, up to large plastic strains, using established test methods (Rathbun et al., 2004). Cell calculations are performed by finite elements that, in association with the measurements, provide a comprehensive characterization of the core response. A constitutive law for the core is devised, based on input from the cell calculations.

(iii) *Panel performance:* Flexural tests with varying end conditions are performed to assess the mechanical performance up to large displacements. Comparisons between experiments and simulations are used to assess the core constitutive law and to make necessary adjustments. Validation of the law is deemed complete once consistency is obtained for various panel geometries and test conditions.

The purpose of the present study is to describe and implement the preceding protocol for a truss core panel with the pyramidal topology (Fig. 1).

2. Sandwich panel design

2.1. Failure mechanism maps

Assessment of the structural performance of a sandwich panel assumes generalized bending (Fig. 1(a)). Performance indices (one based on weight and the other on load) are needed to ascertain minimum weight

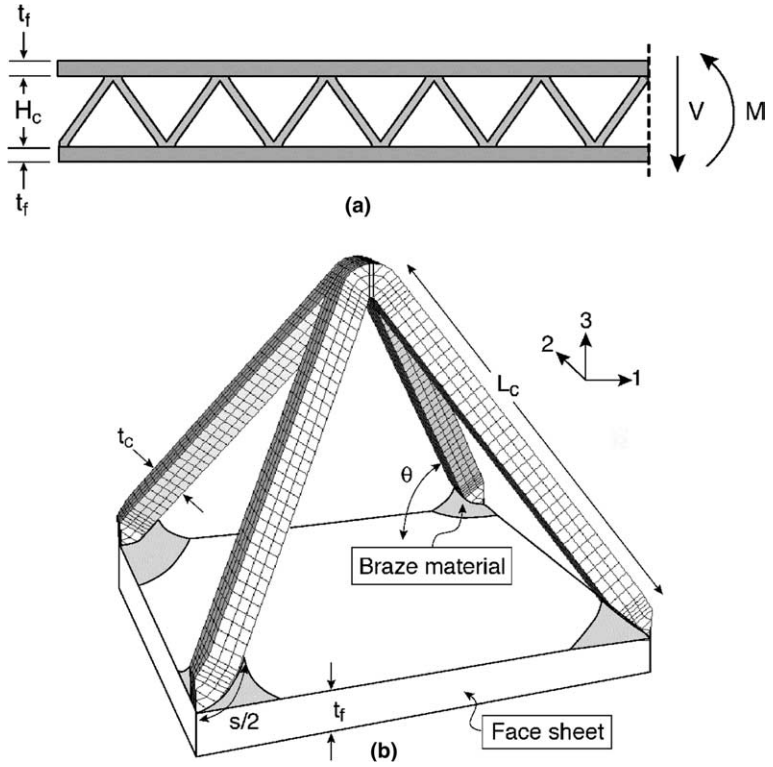

Fig. 1. (a) Sandwich panel and (b) typical unit cell of pyramidal truss core (absent the top face sheet).

configurations and to compare designs. For panels subject to bending over a span S, the load index for strength-based designs can be expressed through a combination of the maximum bending moment, M, and maximum transverse shear, V (both per unit width) (Wicks and Hutchinson, 2001):

$$\Pi_{\mathrm{b}} = \frac{V}{\sqrt{EM}} \tag{1}$$

The ratio of the maximum M and V defines a characteristic length scale, $\ell \equiv M/V$ (Wicks and Hutchinson, 2001). The weight index is [Ashby et al., 2000; Rathbun et al., 2004; Budiansky, 1999; Wicks and Hutchinson, 2001):

$$\Psi = \frac{W}{\rho \ell} \tag{2}$$

where W is the structural weight per unit area and ρ the density of the solid material. Minimum weight designs are found by identifying the failure modes, specifying the load capacity and then varying the dimensions to determine the lowest weight for each mode (Ashby et al., 2000; Wicks and Hutchinson, 2001).

For a sandwich panel with a regular pyramidal core, three independent parameters define the geometry: core thickness, H_{c}, core member width, t_{c} (square section), and face sheet thickness, t_{f} (Fig. 1(b)). The dependent parameters are the core member length, L_{c},

$$L_{\mathrm{c}} = \sqrt{2} H_{\mathrm{c}} \tag{3}$$

and the core relative density, $\bar{\rho}_{\mathrm{c}}$:

$$\bar{\rho}_{\mathrm{c}} = 2\sqrt{2}\left(\frac{t_{\mathrm{c}}}{H_{\mathrm{c}}}\right)^2 \tag{4}$$

The corresponding weight index is:

$$\Psi \equiv \frac{W}{\rho \ell} = 2\frac{t_{\mathrm{f}}}{\ell} + \frac{2\sqrt{2} t_{\mathrm{c}}^2}{H_{\mathrm{c}} \ell} \tag{5}$$

The four possible failure modes for the pyramidal truss core sandwich structure in bending are face sheet yielding, face sheet buckling, core member yielding and core member buckling (Wicks and Hutchinson, 2001). Based on these mechanisms, the constraints (expressed non-dimensionally) are:

$$\left(\frac{V}{\sqrt{EM}}\right)^2 \frac{E}{\sigma_{\mathrm{y}}} \frac{\ell^2}{t_{\mathrm{f}} H_{\mathrm{c}}} \leqslant 1 \quad \text{(face sheet yielding)} \tag{6a}$$

$$\left(\frac{V}{\sqrt{EM}}\right)^2 \frac{24(1-\nu^2)}{k\pi^2} \frac{H_{\mathrm{c}} \ell^2}{t_{\mathrm{f}}^3} \leqslant 1 \quad \text{(face sheet buckling)} \tag{6b}$$

$$\left(\frac{V}{\sqrt{EM}}\right)^2 \frac{E}{\sigma_{\mathrm{y}}} \frac{H_{\mathrm{c}} \ell}{t_{\mathrm{c}}^2} \leqslant 1 \quad \text{(core member yielding)} \tag{6c}$$

$$\left(\frac{V}{\sqrt{EM}}\right)^2 \frac{24}{k\pi^2} \frac{H_{\mathrm{c}}^3 \ell}{t_{\mathrm{c}}^4} \leqslant 1 \quad \text{(core member buckling)} \tag{6d}$$

where σ_{y} is yield strength and E is Young's modulus. The parameter k depends on the level of end constraint during buckling; for pin-jointed connections, $k = 1$. This selection leads to conservative estimates of load bearing capacity.

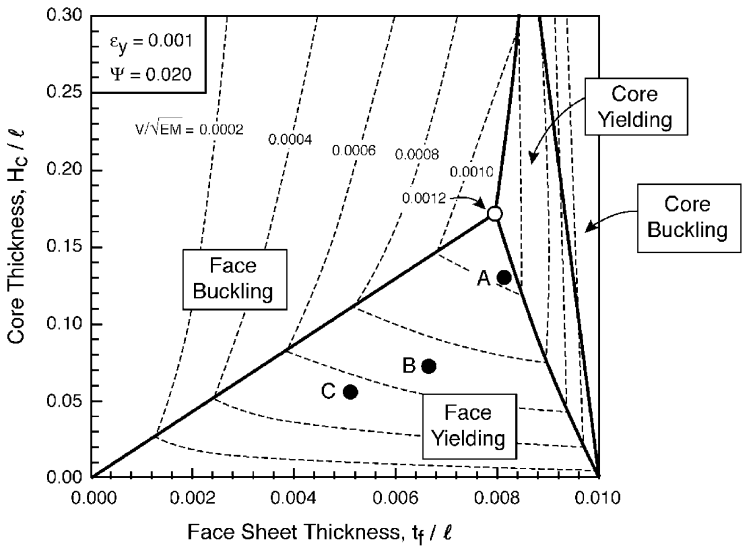

Fig. 2. Failure mechanism map for pyramidal core sandwich panel with fixed weight. The solid circles labeled A, B and C correspond to the parameter values used in the experiments.

The preceding analysis can be used to generate failure mechanism maps. For designs of constant weight, the core thickness, t_c/ℓ, is eliminated from the constraint functions (via Eq. (5)), allowing the maps to be rendered in coordinates H_c/ℓ and t_f/ℓ. The domain boundaries are obtained by sequentially equating pairs of constraint functions. Within each domain, the load bearing capacity is calculated from Eqs. (6a)–(6d) and the results superimposed on the maps as a family of constant strength contours. One such map, for weight $\Psi = 0.02$ and yield strain $\varepsilon_y = 0.001$, is shown in Fig. 2. The coordinates of the optimal configuration (with largest load capacity) are obtained at the confluence of face sheet yielding, face sheet buckling and core member yielding.

2.2. Design optimization

The analysis is extended to obtain the entire family of optimal designs. The designs are ascertained by following standard procedures in the minimization of the objective function (notably, the weight), subject to multiple constraints (Eqs. (6a)–(6d)). Operationally, the optimization is carried out by stepping through values of the load index, $V/\sqrt{EM}$, and solving for the geometric parameters (t_c/ℓ, H_c/ℓ and t_f/ℓ) that yield minimum weight (Wicks and Hutchinson, 2001; Zok et al., 2003).

The optima are obtained at the confluence of three failure mechanisms. At low load capacity, these mechanisms are face yielding, face buckling and core buckling: whereupon the optimal parameter values and the minimum weight are given by:

$$\frac{H_c}{\ell} = \left(\frac{E}{\sigma_y}\right)^{3/4} \left(\frac{\pi^2}{24(1-\nu^2)}\right)^{1/4} \frac{V}{\sqrt{EM}} \tag{7a}$$

$$\frac{t_f}{\ell} = \left(\frac{24(1-\nu^2)E}{\pi^2\sigma_y}\right)^{1/4} \frac{V}{\sqrt{EM}} \tag{7b}$$

$$\frac{t_c}{\ell} = \left(\frac{24}{\pi^2(1-\nu^2)^3}\right)^{1/16}\left(\frac{E}{\sigma_y}\right)^{9/16}\left(\frac{V}{\sqrt{EM}}\right)^{5/4} \tag{7c}$$

$$\Psi = \left(\frac{384(1-\nu^2)E}{\pi^2\sigma_y}\right)^{1/4}\left(\frac{V}{\sqrt{EM}}\right) + \frac{9.31}{(1-\nu^2)^{1/8}\pi^{3/4}}\left(\frac{E}{\sigma_y}\right)^{3/8}\left(\frac{V}{\sqrt{EM}}\right)^{3/2} \tag{7d}$$

At high load, core buckling replaces core yielding as one of the failure modes. The transition to buckling occurs at a load capacity:

$$\left(\frac{V}{\sqrt{EM}}\right)_{tr} = \frac{24^{3/4}}{(1-\nu^2)^{1/4}\pi^{3/2}}\left(\frac{\sigma_y}{E}\right)^{5/4} \tag{8}$$

Replacement of core buckling by core yielding alters the core member thickness and the minimum weight, now given by:

$$\frac{t_c}{\ell} = \left(\frac{\pi^2}{24(1-\nu^2)}\right)^{1/8}\left(\frac{E}{\sigma_y}\right)^{7/8}\left(\frac{V}{\sqrt{EM}}\right)^{3/2} \tag{9a}$$

$$\Psi = \left(\frac{384E(1-\nu^2)}{\pi^2\sigma_y}\right)^{1/4}\left(\frac{V}{\sqrt{EM}}\right) + 2\sqrt{2}\frac{E}{\sigma_y}\left(\frac{V}{\sqrt{EM}}\right)^2 \tag{9b}$$

The results for core thickness and face sheet thickness remain unchanged (Eqs. (7a) and (7b)).

Left unconstrained, the optimal core thickness increases monotonically with load capacity, eventually departing the domain of thin panels. Restricting the core thickness to a maximum value $(H_c/\ell)^{max}$, the optimal values of the remaining parameters and the weight become:

$$\frac{t_f}{\ell} = \left(\frac{V}{\sqrt{EM}}\right)^2\frac{E}{\sigma_y}, \frac{1}{(H_c/\ell)^{max}} \tag{10a}$$

$$\frac{t_c}{\ell} = \left(\frac{V}{\sqrt{EM}}\right)\left[\frac{E}{\sigma_y}\left(\frac{H_c}{\ell}\right)^{max}\right]^{1/2} \tag{10b}$$

$$\Psi = \frac{2E}{\sigma_y}\left(\frac{V}{\sqrt{EM}}\right)^2\left[\frac{1}{(H_c/\ell)^{max}} + \sqrt{2}\right] \tag{10c}$$

The corresponding load at the transition to thickness-limited design is:

$$\left(\frac{V}{\sqrt{EM}}\right)_{tr} = \varepsilon_y^{3/4}\left(\frac{24(1-\nu^2)}{\pi^2}\right)^{1/4}\left(\frac{H_c}{\ell}\right)^{max} \tag{11}$$

The results from one such set of calculations, for yield strain $\varepsilon_y = 0.001$, are shown in Fig. 3. Also shown for comparison is the weight of a solid sheet of the same material, given by (Zok et al., 2003):

$$\Psi_s = \left(\frac{6E}{\sigma_y}\right)^{1/2}\frac{V}{\sqrt{EM}} \tag{12}$$

The weight benefits of the sandwich panel over the solid plate are evident.

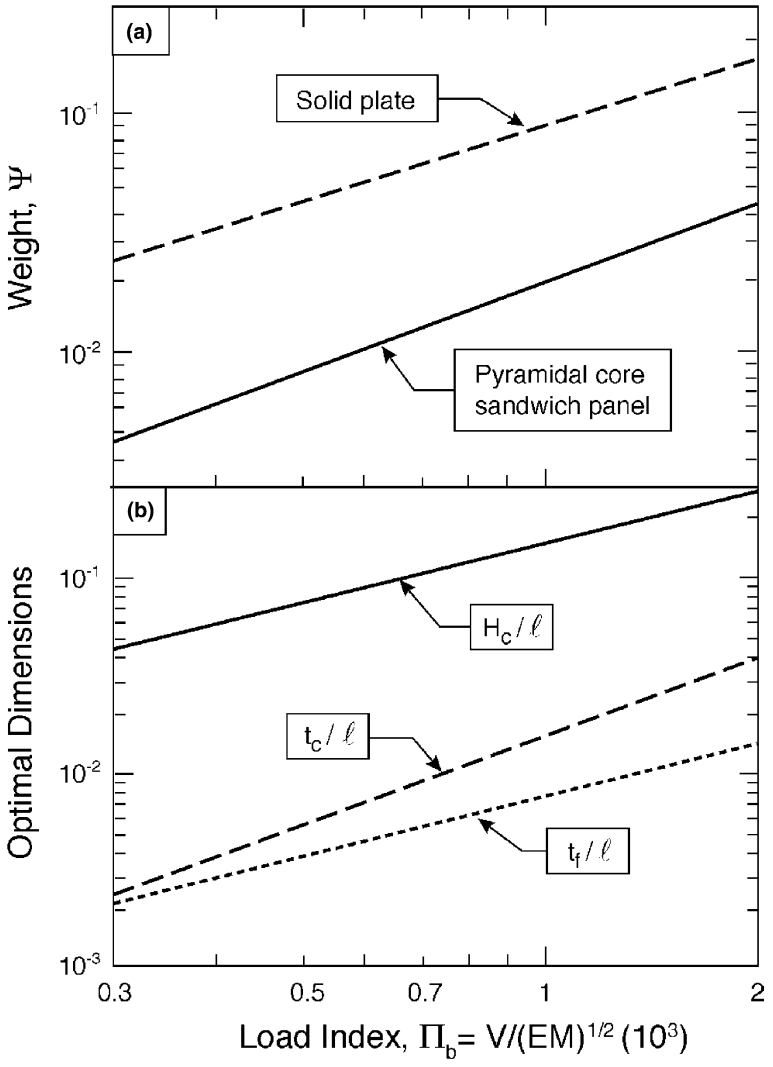

Fig. 3. Weight and dimensions of optimized pyramidal core sandwich panel.

2.3. Panel design and fabrication

The failure maps and design optimizations have been used to devise experiments that probe the core and panel responses in the vicinity of the optimum. To ensure robust response subsequent to failure initiation, the preferred designs lead to failure by *yielding* (rather than elastic buckling) of either the core or the face sheets. Three sets of design parameters have been selected for use in subsequent experiments, each with the same weight per unit area. The parameter values are summarized in Table 1. When tested in three-point bending with a loading span $S = 184$ mm, their non-dimensional weight becomes $\Psi = 0.02 \pm 0.002$. The experimental points are superimposed on the mechanism map in Fig. 2. All two configurations reside within the face yielding domain, although the one denoted A lies close to the boundary between face and core yielding. The predicted strengths fall in the range $V/\sqrt{EM} \approx 0.0005$–$0.0010$. By comparison, the predicted optimum is at $V/\sqrt{EM} = 0.0012$.

Table 1
Summary of sandwich panel design parameters

Panel designation	Face sheet thickness, t_f (mm)	Core member width, t_c (mm)	Core thickness, H_c (mm)	Core relative density, $\bar{\rho}_c$	Weight[a], $(2t_f + \bar{\rho}_c H_c)\rho$ (kg/m^2)	Normalized weight[b], Ψ
A	0.76	1.22	11.5	0.027	14.8	0.020
B	0.64	1.22	6.71	0.079	14.0	0.0195
C	0.51	1.22	5.28	0.121	13.3	0.018

[a] ρ is the density of 304 stainless steel: 7800 kg/m^3.
[b] Corresponds to three point bending with a span $S = 184$ mm, whereupon $\ell = S/2 = 92$ mm.

Sandwich panels were fabricated using 304 stainless steel for both the core and the face sheets. To produce a core, a periodic array of diamond-shaped holes was laser cut into a flat sheet such that the intervening ligaments produced square truss members. The sheet was sequentially bent along the lines of the nodes through an angle of 60°, thereby forming a regular pyramidal truss structure (Fig. 4). Typical in-plane dimensions were 150 mm×200 mm. Cores were subsequently bonded to the face sheets by brazing. This was accomplished by first dipping the nodes of the cores into a mixture of a polymer-based cement (Nicrobraz Cement 520) and a Ni–22Cr–6Si braze powder (Nicrobraz 31), both supplied by Wal Colmonoy (Madison Heights, MI). The cores were then placed between the face sheets, a light load was applied to ensure contact, and the assembly heated in a vacuum furnace for 2 h at 1075 °C. To enable gripping in the clamped bending experiments (described in Section 4), solid steel inserts had been brazed to the face sheets at the two ends of the panels, each over a length of 75 mm. For assessment of panel performance, the face sheet thicknesses were selected in accordance with the values in Table 1. For measurement of the core properties, both in shear and in compression, the face sheets were considerably thicker (2 mm), to ensure adequate core constraint during testing.

The resultant structure of each core unit is depicted on Fig. 1. Bending of the core members, followed by brazing, generates the nodal configuration depicted on the figure. That is, a fillet of braze material connects the core to the faces over a length, s. It will be shown that the ratio, s/t_c, affects the compressive and shear response of the core.

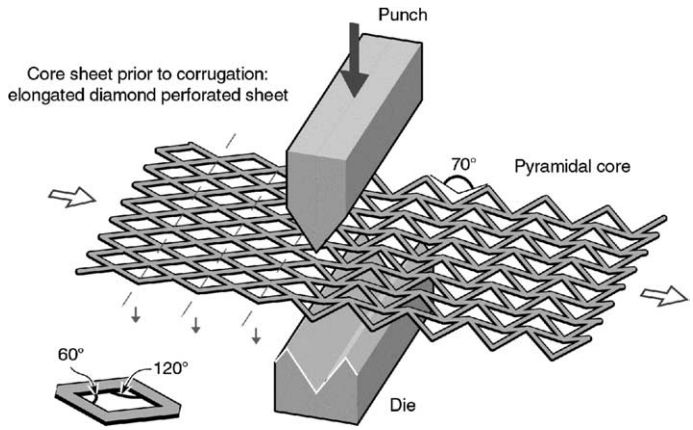

Fig. 4. Cutting and bending operations used to fabricate pyramidal truss cores.

3. Core characterization

3.1. Synopsis

A perspective is provided by typical simulation results, with details to follow. It will be shown that, for the pyramidal truss, the core can be characterized by three tests: transverse compression, σ_{33} (Fig. 5a), in-plane shear, σ_{13} (Fig. 5b), and in-plane tension, σ_{11} (Fig. 5c). Analytical results for these tests define the orthotropy (Xue and Hutchinson, 2004). They depend principally on the relative core density and the angle θ between the core members and the face sheets. For $\theta = 45°$, the non-dimensional elastic constants are:

$$\frac{E_{33}}{E\bar{\rho}_c} = \sin^4\theta \approx 0.25 \tag{13a}$$

$$\frac{G_{13}}{E\bar{\rho}_c} = \frac{G_{23}}{E\bar{\rho}_c} = \frac{1}{8}\sin^2 2\theta \approx 0.125 \tag{13b}$$

Initial yield occurs at the non-dimensional stresses ($\theta = 45°$):

$$\frac{\sigma^0_{33}}{\sigma_y\bar{\rho}_c} = \sin^2\theta = 0.5 \tag{14a}$$

$$\frac{\sigma^0_{13}}{\sigma_y\bar{\rho}_c} = \frac{\sigma^0_{23}}{\sigma_y\bar{\rho}_c} = \frac{1}{2\sqrt{2}}\sin 2\theta \approx 0.35 \tag{14b}$$

$$\frac{\sigma^0_{11}}{\sigma_y\bar{\rho}_c} = \frac{\sigma^0_{22}}{\sigma_y\bar{\rho}_c} = \frac{1}{2}\sqrt{\bar{\rho}_c}\,\frac{\tan^2\theta\sin^{5/2}\theta}{\sqrt{\sin^2\theta + (1/2)\cos^2\theta}} \approx 0.24\sqrt{\bar{\rho}_c} \tag{14c}$$

Simulated stress/strain curves for these three tests performed at a core density, $\bar{\rho}_c = 0.073$, are summarized on Fig. 6. Consistent with Eq. (14), the compressive yield strength is the highest and the in-plane stretch strength the lowest. Beyond yield, appreciable strain hardening occurs, both in compression and in shear. At strains larger than about 0.2, the compressive stress reaches a peak and diminishes below the shear strength, with the in-plane stretch strength remaining the lowest. The magnitude of the compression peak depends on $\bar{\rho}_c$. At low $\bar{\rho}_c$, it is associated with the onset of plastic buckling and occurs just beyond yield. At larger $\bar{\rho}_c$, the material continues to strain harden, even after the truss starts to buckle: a response typical of stubby columns (Xue and Hutchinson, 2004). In compression, at high strains, the deformed trusses contact the faces and, thereafter, the core hardens rapidly as it densifies.

One of the findings of the following assessment is that consistent discrepancies arise between measurements and simulations, both when ascertaining core properties and upon panel bending. The primary source of the disparity appears to involve some uncertainty in the constituent mechanical properties of the core members and of the faces after fabrication. That is, while tensile tests have been performed on the same material (304 stainless steel in this instance) subject to the same thermal cycle used in fabrication, the final properties of the material in the assembled panel appear to differ. An assessment of this effect was made by brazing pairs of thin sheets of 304 stainless steel, following the same procedure used for panel fabrication, and subsequently measuring their tensile properties. To determine the role of the "braze concentration", two sheet thicknesses were used, 0.254 mm and 0.190 mm, yielding total sample thicknesses, $2t = 0.51$ mm and 0.38 mm. (Because the amount of braze was exceedingly small, the final thickness was essentially equivalent to that of the two sheets combined, within measurement uncertainty.) The results of the tensile tests are plotted on Fig. 7. Evidently, the braze increases the flow stress of the alloy, by as much as 30%. Furthermore, its magnitude increases with the braze concentration, as manifested in the dependence on

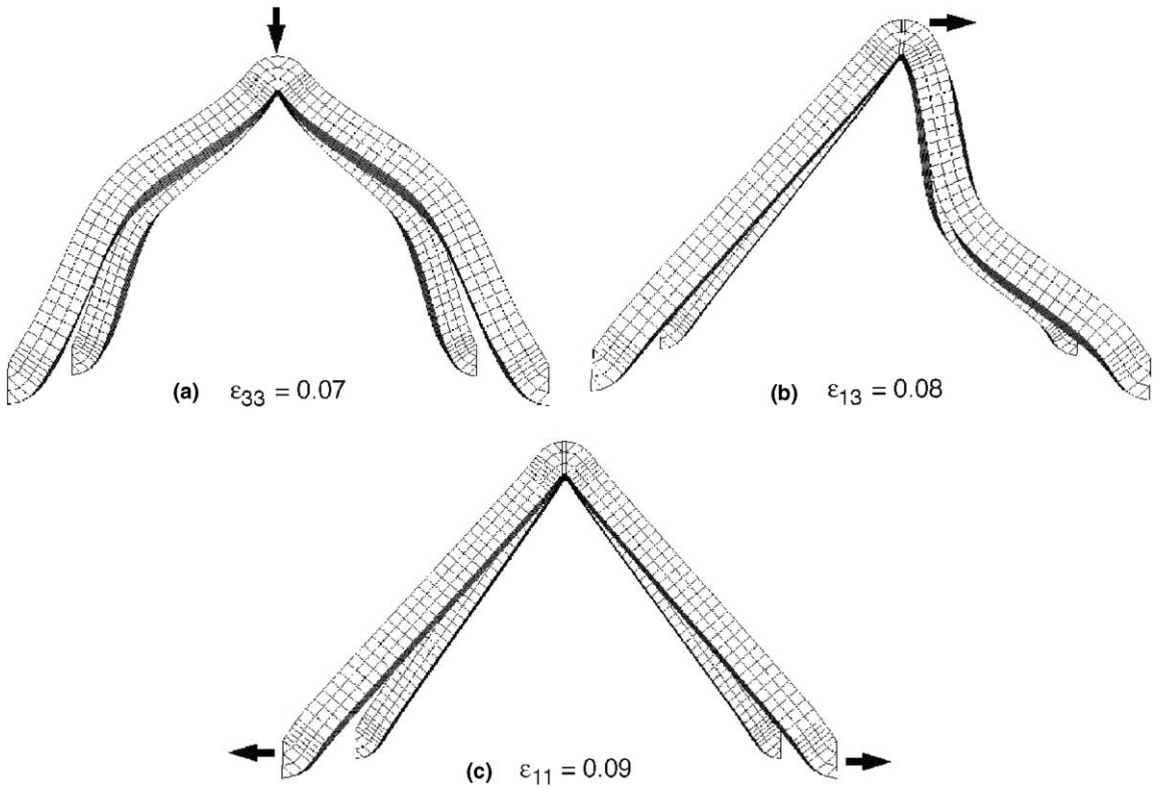

Fig. 5. Representative cell calculations used to calibrate core constitutive law: (a) transverse compression, (b) shear, and (c) in-plane tension.

sheet thickness. Because the spatial distribution of braze is non-uniform in the sandwich panels, a quantitative correction to the average flow properties of the steel cannot be ascertained. In principle, the properties can be inferred by fitting one set of finite element simulations to the corresponding measurements. This procedure has yet to be implemented.

3.2. Constitutive law

The simplest orthotropic constitutive law is an embellishment of that suggested by Hill, characterized by an effective stress σ_e (Xue and Hutchinson, 2004; Hill, 1948):

$$2\sigma_e^2 = \alpha_{12}(\sigma_{11}-\sigma_{22})^2 + \alpha_{23}(\sigma_{22}-\sigma_{33})^2 + \alpha_{31}(\sigma_{33}-\sigma_{11})^2 + 6\alpha_{44}\sigma_{12}^2 + 6\alpha_{55}\sigma_{23}^2 + 6\alpha_{66}\sigma_{31}^2 + \alpha_{11}\sigma_{11}^2 + \alpha_{22}\sigma_{22}^2 + \alpha_{33}\sigma_{33}^2 \tag{15}$$

The coefficients, α_{ij}, dictate the anisotropy of yielding and its relative sensitivity to shear and pressure. The yield criterion is

$$f = \sigma_e - \sigma_0 = 0 \tag{16}$$

where σ_0 is the uniaxial yield strength. This law prescribes smooth yield surfaces (no corners). While this simplification is deficient for the generalized loading of truss topologies (such as the octet truss) (Deshpande

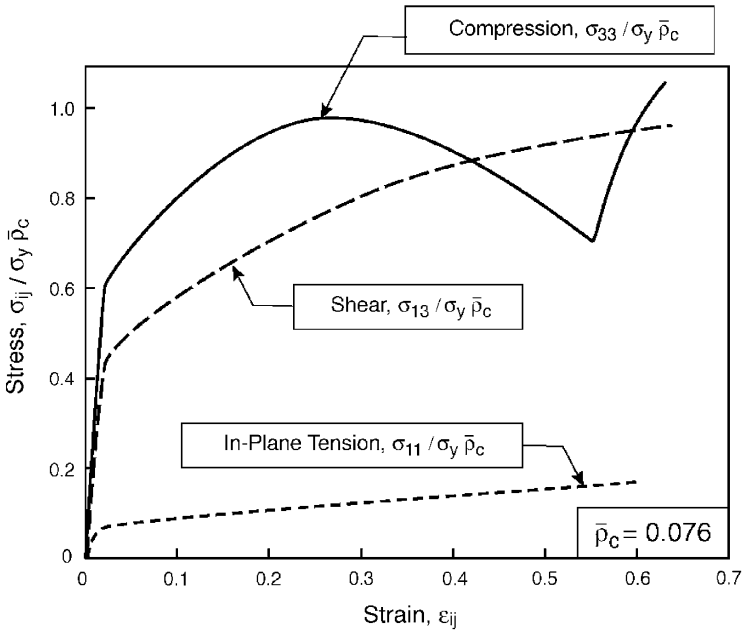

Fig. 6. Representative results from finite element simulations, showing the general features associated with yielding and subsequent hardening/softening for each of the three loadings.

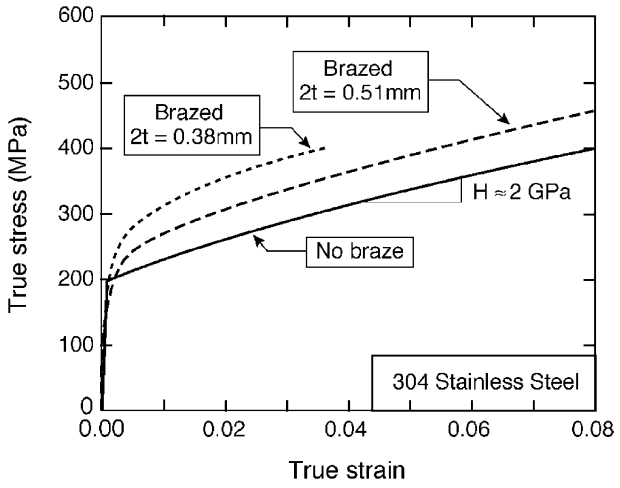

Fig. 7. Tensile response of 304 stainless steel, after annealing (solid line) and upon brazing (dashed lines).

et al., 2001), it may be adequate for the more limited range of stress space applicable to sandwich structures. Furthermore, the hardening rule assumes that the yield surface does not change in shape as the yield stress is exceeded.

The coefficients, α_{ij}, can be determined either by numerical simulation or by experiment, or both. For present purposes, the same approximation introduced by Xue and Hutchinson (2004) is used: namely, that

the plastic and elastic Poisson ratios are zero. The consequence is that $\alpha_{12} = \alpha_{23} = \alpha_{31} = 0$. The implications are discussed elsewhere (McMeeking, in press). For pyramidal cores, $\alpha_{11} = \alpha_{22}$ and $\alpha_{13} = \alpha_{23}$. Moreover, for panels tested in bending, the out-of-plane shear loads are zero, so that α_{12} is not relevant. The remaining α_{ij} coefficients can be ascertained from results obtained using transverse compression, σ_{33}, in-plane shear, σ_{13}, and in-plane tension, σ_{11}.

Finite element calculations are performed using the shapes of trusses and nodes developed by bending and brazing. A typical mesh is shown on Fig. 1. A variable in the calculations is the attachment length ratio, s/t_c, because the fillet varies between nodes and between manufacturing runs. The range is from narrow, $s/t_c = 2$ (case A) to broad, $s/t_c = 4$ (case B). The analysis is performed by using 8-node linear solid elements with reduced integration (designated C3D8R). The calculations use a bilinear representation of the stress/strain curve for 304 stainless steel, with yield strain, $\varepsilon_y = 10^{-3}$, and hardening modulus, $H = 2.0$ GPa (Fig. 7).

Boundary conditions are chosen that account for the attachment of the core to the faces. That is, the surface length s is considered to be rigid with no rotation. In transverse compression, the base is fixed, both horizontally and vertically, and the apex displaced downward (without rotation). These conditions induce in-plane stresses that elevate σ_{33}. In-plane shear calculations are performed by displacing the apex in the horizontal plane, without rotation, while fixing the base. The apex is allowed to displace downward to assure zero vertical force. For in-plane tension, the apex is fixed, both vertically and horizontally. In plane stretch is imposed on the members at the base, with no rotation, allowing through thickness displacements that assure zero vertical force. The deformations associated with each of the three load conditions are evident in the simulated shapes (Fig. 5). Note the incidence of plastic buckling of the compressed members in both compression and shear. In compression, at large strains, contact occurs between the core members and the faces.

Calculations for in-plane shear and tension are carried out using an implicit finite element code (ABAQUS-Standard). In contrast, for transverse compression, the calculations are performed using an explicit code (ABAQUS-Explicit), to take advantage of its superior ability to handle contact problems. For the latter calculations, two rigid surfaces are added to represent the face sheets. At large deformations, contacts occur between these surfaces and the trusses as well as between neighboring trusses. All contacts are assumed to be frictionless. (Implicit codes generally are not effective for problems with complex contacts and convergence problems are often encountered.) For the computations using the explicit code, the lowest natural frequency of vibration of the elastic model was first computed. The loading rate for plastic crushing was then chosen to ensure that the maximum deformation was reached much later than 10 periods of vibration at the computed frequency. This slow loading rate coupled to the dissipation due to plasticity ensured that the explicit code delivered essentially a quasi-static response. The absence of significant oscillations in the resulting load–deflection curves confirms the validity of the approach.

Calculations have been performed for four relative densities, in the range probed experimentally ($\bar{\rho}_c = 2.6\%$, 4.0%, 7.3%, 11%). The emphasis is on the plastic strains.

3.3. Properties

3.3.1. Transverse compression

The stress/(plastic) strain curves obtained by measurement and by simulation are summarized on Fig. 8. The associated shape deformations of the trusses, ascertained by simulation, are presented on Fig. 9. All of these cores yield at $\sigma_{33}/\sigma_y\bar{\rho}_c \approx 0.5$, followed shortly by plastic buckling. (Note that, in materials with higher yield strain, the lowest density cores would be susceptible to elastic buckling). At the larger relative densities ($\bar{\rho} \geqslant 7\%$), strain hardening continues up to strains of order 20–30%, despite plastic buckling, because of the stubbiness of the truss members (Cote et al., 2004; Hill, 1948). At large strains, the distorted truss members contact the faces (Fig. 9), initiating rapid hardening and densification. At small relative densities ($\bar{\rho}_c \leqslant 4\%$),

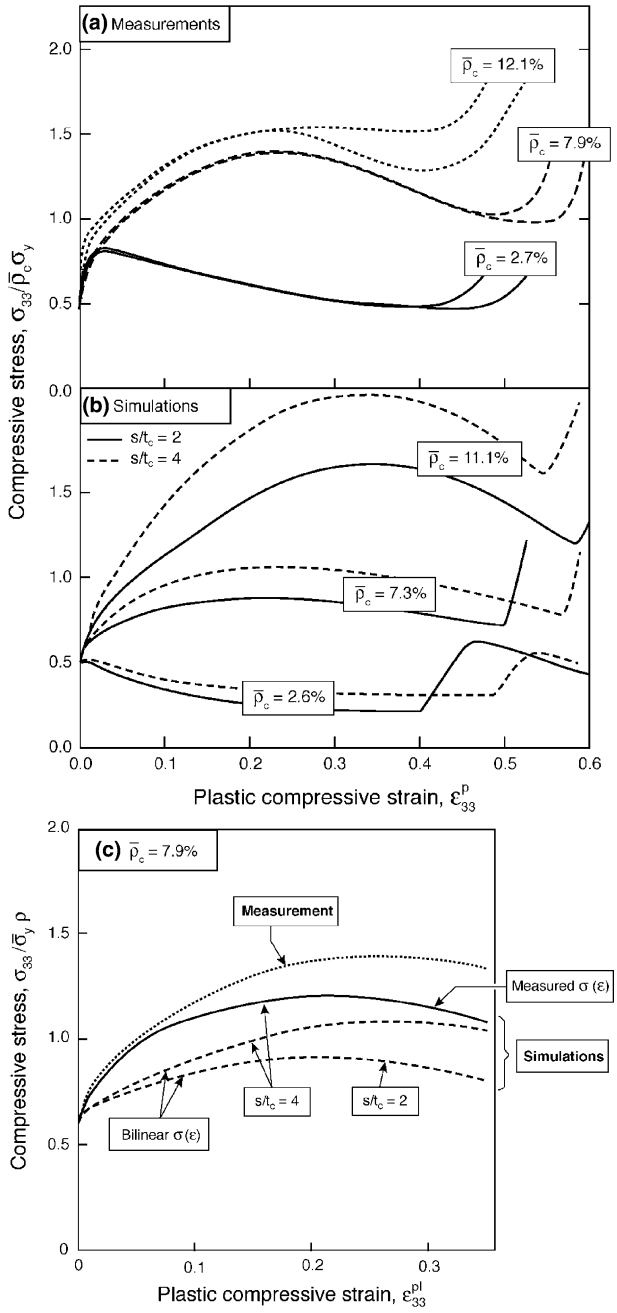

Fig. 8. Compressive response of pyramidal truss cores, from both experiments and simulations.

the plastic buckling leads to gradual softening shortly after yielding, followed by an extensive plateau. Initial contact between the core members and the faces is restricted in extent (Fig. 9), resulting in only a small transient load elevation (Fig. 8a). Further deformation is needed to induce the extensive contact that causes rapid hardening and densification evident at higher densities.

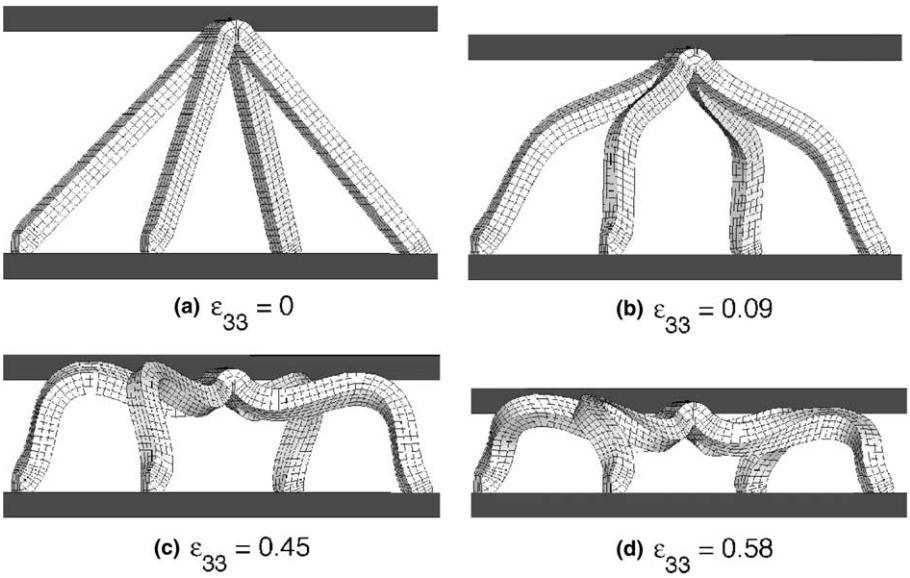

Fig. 9. Shape change of truss elements during compressive loading, for core with $\bar{\rho}_c = 2.6\%$.

Inspection of the figures indicates that the trends in the measurements (Fig. 8a) are similar to those ascertained by simulation (Fig. 8b and c), but discrepancies remain. At the lowest density, $\bar{\rho}_c \approx 2.6\%$, contrary to the simulations, the measured curves display strain hardening after yield, before the onset of plastic buckling and softening. A similar disparity has been discerned in studies of square honeycomb cores (Cote et al., 2004). A more detailed comparison, performed at the intermediate relative density (Fig. 8c), reveals the sensitivity of the simulated curves to the attachment length, s/t_c, and to the input stress/strain, $\sigma(\varepsilon)$, curve for the material (measured versus bilinear). The closest correspondence with the measurements obtains at the larger $s/t_c = 4$ and when the measured (rather than bilinear) $\sigma(\varepsilon)$ curve is used as input. Accordingly, in future assessments, the actual $\sigma(\varepsilon)$ will be used instead of the bilinear approximation. Even then, adjustments to the actual flow stress (while retaining the hardening exponent) might still be needed to account for property changes caused by manufacturing.

3.3.2. In-plane shear

The calculated and measured shear stress/strain curves are summarized on Fig. 10 and the shape deformations on Fig. 11. The numerical results indicate that all cores yield at a stress, $\sigma_{13}/\sigma_y\bar{\rho}_c \approx 0.4$, followed by strain hardening. At the higher relative densities, $\bar{\rho}_c \geqslant 7\%$, even though the core members in compression buckle plastically (Fig. 11), the stubbiness of the truss members allows continued strain hardening. The hardening continues until the loads are removed. At lower relative densities, the core members in compression buckle plastically soon after yielding, resulting in softening and continued deformation at a "plateau" stress of order, $\sigma_{13}/\sigma_y\bar{\rho}_c \approx 0.4$.

The experiments again differ in various respects from the simulations. At the higher densities, the measured hardening rate exceeds that obtained by simulation. The closest correspondence is again reached when the larger contact, $s/t_c = 4$, and the measured stress/strain curve are used in the simulations. The experiments at these densities exhibit load drops at stresses of $\sigma_{13}/\sigma_y\bar{\rho}_c \approx 0.8$, because some of the nodes rupture. Rupture mechanisms have yet to be included in the FE model.

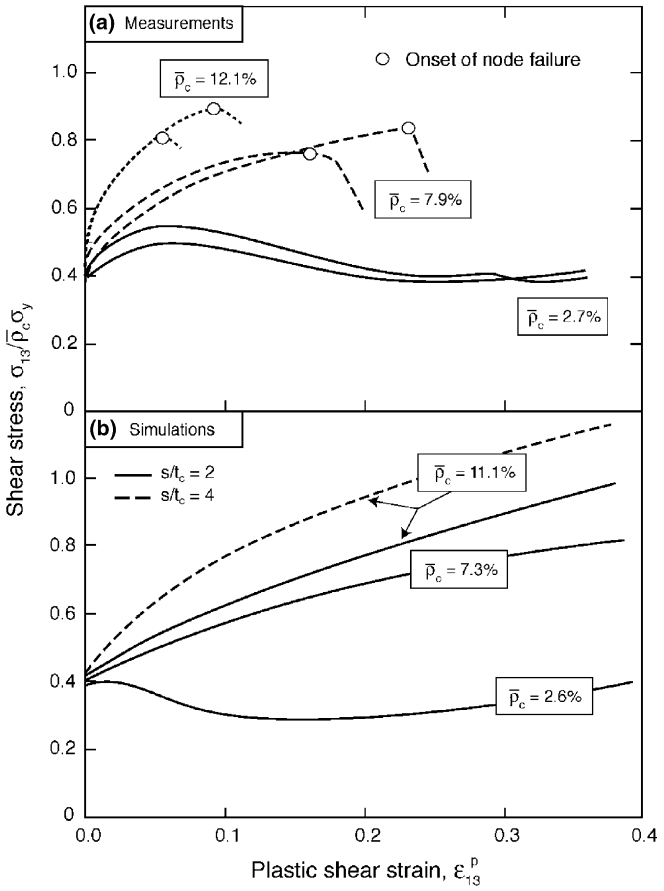

Fig. 10. Shear response of pyramidal truss cores, from both experiments and simulations.

3.3.3. In-plane tension

The simulations reveal that the core exhibits a stress–strain response (Fig. 6), proportional to that of the steel (Fig. 7). By analogy to the analytical results in Eq. (14), its stretch resistance can be characterized by a non-dimensional parameter:

$$\beta = \frac{\bar{\sigma}_{11}}{\bar{\rho}_c \bar{\sigma}_f} \tag{17}$$

where $\bar{\sigma}_{11}$ and $\bar{\sigma}_f$ represent the flow stresses of the core and the face, respectively, at a prescribed strain. In general, it can vary over the range $0 \leqslant \beta \leqslant 1$. For $\bar{\rho}_c = 0.073$, $\beta = 0.07$ (Fig. 6): consistent with the analytical prediction for the onset of yield, given in Eq. (14c).

In-plane tensile tests on the sandwich panels reveal a similarly low stretch resistance for the core (Fig. 12). In this context, the relevant tensile stress is the load, F, normalized by the area density, BH_{eq} (where B is the width and H_{eq} is the thickness of a solid plate at the same mass). The flow stress of the sandwich panel is partitioned between the core and the face sheets, each weighted by its respective thickness. The resulting panel strength is:

$$\bar{\sigma}_{panel} \equiv \frac{F}{BH_{eq}} = \bar{\sigma}_f \left[(1-\beta)\left(\frac{2t_f}{H_{eq}}\right) + \beta \right] \tag{18}$$

A fit of the measurements to this formulation indicates that $\beta \approx 0.1$ (Fig. 12).

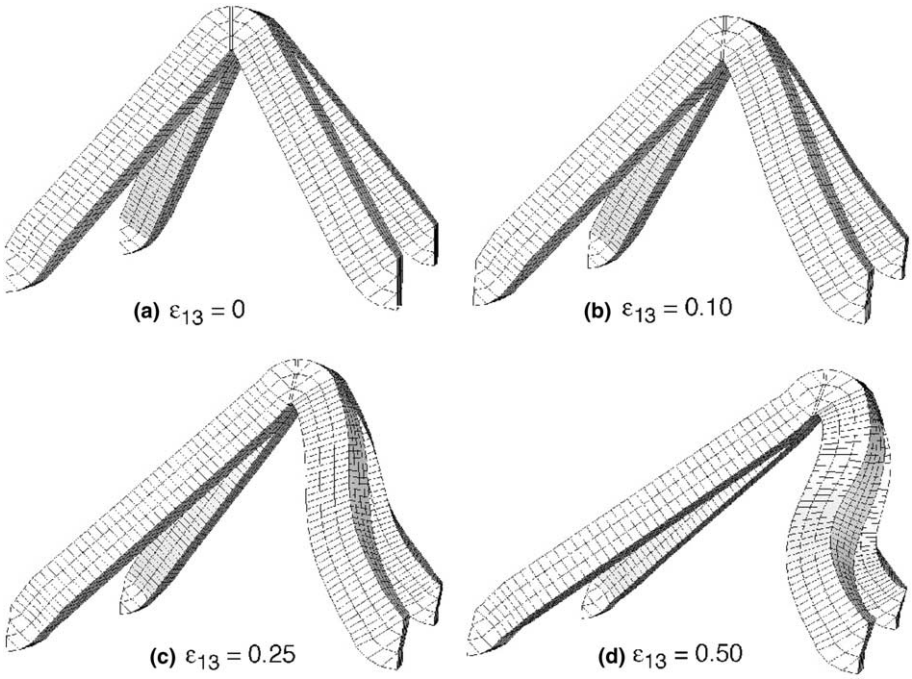

Fig. 11. Shape change of truss elements during shear loading, for core with $\bar{\rho}_c = 7.3\%$.

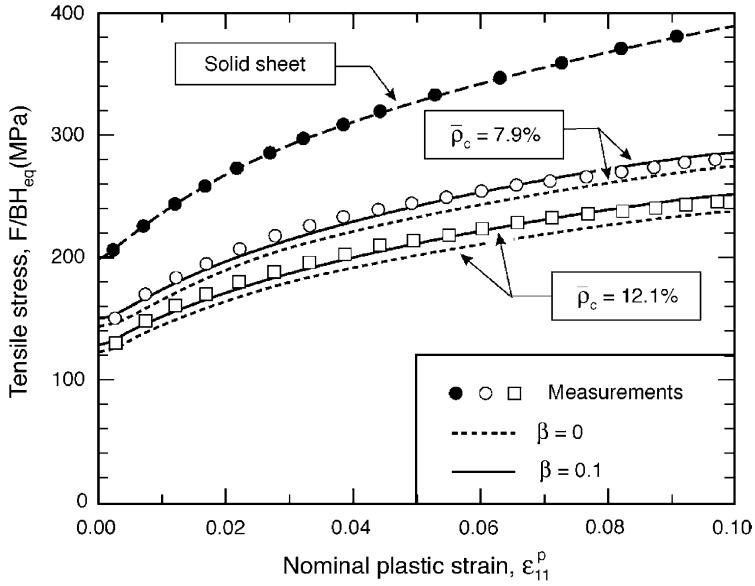

Fig. 12. In-plane tensile response of sandwich panels and solid sheet. The solid and dotted lines show fits of Eq. (18) to the measurements, yielding the indicated values of β.

3.4. Calibration of constitutive law

The stress/strain response beyond initial yield differs for all three loading modes (even when normalized by the initial yield strength, $\sigma_{ij}(\varepsilon_{pl})/\sigma_{ij}(0)$). Yet, the constitutive law can only be implemented by inputing one complete stress/strain curve. To contend with this limitation, the following procedure is utilized. The required α_{ij} are first obtained from the analytic formulae, giving: $\alpha_{33} = 2, \alpha_{13} = \alpha_{23} = 2\sqrt{2}$, $\alpha_{11} = \alpha_{22} = 2^{9/4}\sqrt{3}/\bar{\rho}_c^{1/2}$. Then, the pertinent stress/strain curve is input, based on the most prominent core failure mechanism. In principle, the choice can be informed by referring to failure mechanism maps that incorporate failure by core shear and by core crushing. The implicit assumption is that the subsequent hardening (as well as softening and densification) will be the same in all modes. The ensuing simulations are performed using the compression curves as input.

4. Sandwich panel performance

4.1. Measurements

An assessment of panel performance was made using three-point flexure tests, with one of two end conditions: simply supported or fully clamped. The latter configuration is shown in Fig. 13; an identical configuration was used for the simply supported condition, but without end clamps. The measurements are plotted on Figs. 14a and 15a.

For the simply supported case, the loads and the displacements have been normalized by those needed to initiate yielding in a solid panel of equivalent weight. On this basis, it is evident that the sandwich panels exhibit very much higher bend strengths: up to about 15 times that of the solid at failure initiation (characterized by the onset of non-linearity). The predicted strengths from the analytical model presented in Section 2.1 (shown by open circles in Fig. 14b) agree well with the measurements. The panels exhibit strain hardening after yielding, eventually attaining a load maximum at the onset of plastic buckling of the face sheets (Fig. 16). Face buckling does not occur in the clamped bending tests, because of the membrane (tensile) stresses that arise once the deflections exceed a significant fraction of the panel thickness. Note that the panel with lowest core density ($\bar{\rho}_c = 2.5\%$) has the highest load capacity, because this design is closest to the optimum (Fig. 2).

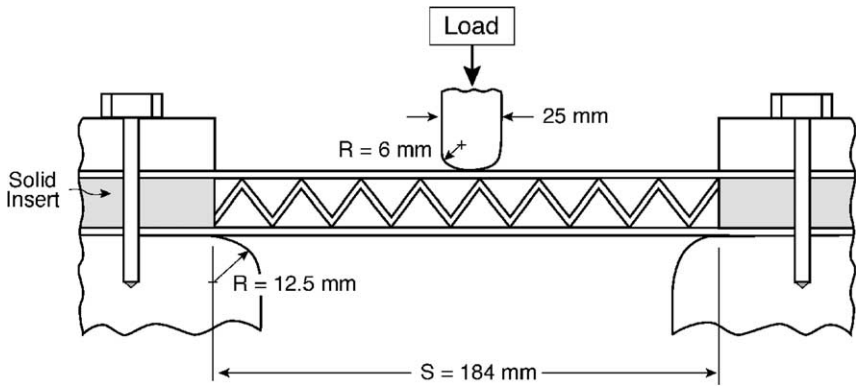

Fig. 13. Schematic of the clamped bending configuration. The same loading configuration was used for the simply-supported bending tests, but without the end clamps.

4.2. Simulations

Panel bending is simulated by using the constitutive law with the transverse compression stress/strain curve as the input for the core. To facilitate convergence, the mesh density for the core is much lower than that for the faces: the former involving two layers of 4-node plane strain continuum elements (CPE4R). This feature precludes the possibility of strain localization occurring in the finite element computations at large strains (wherein the trusses exhibit strain softening) and the associated sensitivity of the results to element size and orientation. Moreover, it ensures that the response of the finite element representing the core during softening has fidelity to the simulated unit cell behavior. That is, the single finite element properly represents the core unit cell; a refinement of the mesh would incorrectly imply an anomalously small unit cell.

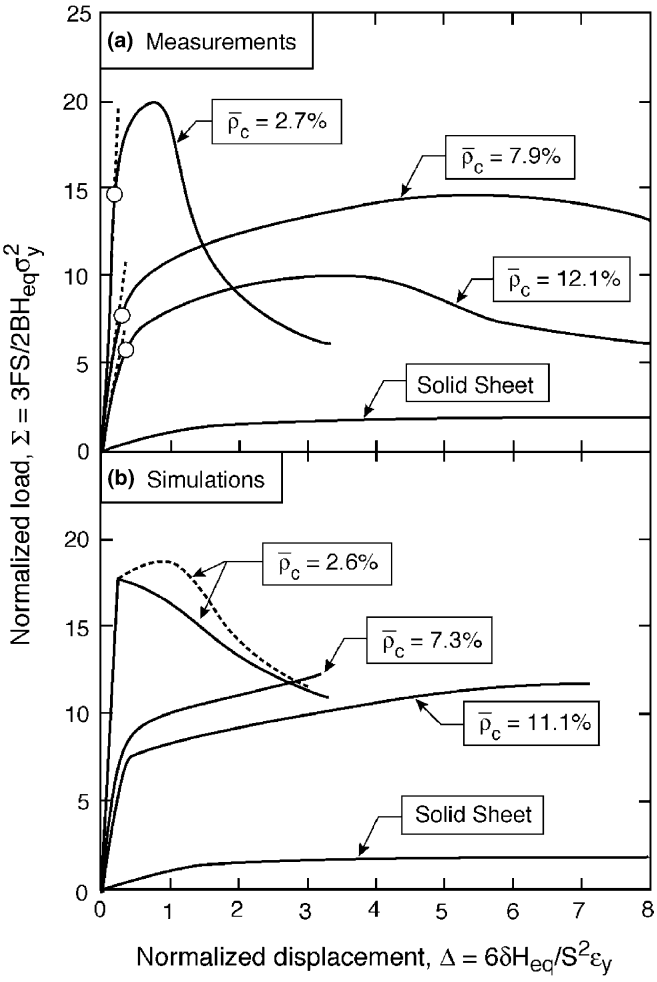

Fig. 14. Simply-supported bending response of sandwich panels. Open circles in (a) are the predicted values for failure initiation, based on the analytical model in Section 2.1. Solid lines in (b) are based on simulations in which the core constitutive law had been calibrated using the *simulated* compressive stress–strain curve; in contrast, the dotted line is based on a calibration from the *measured* compressive response.

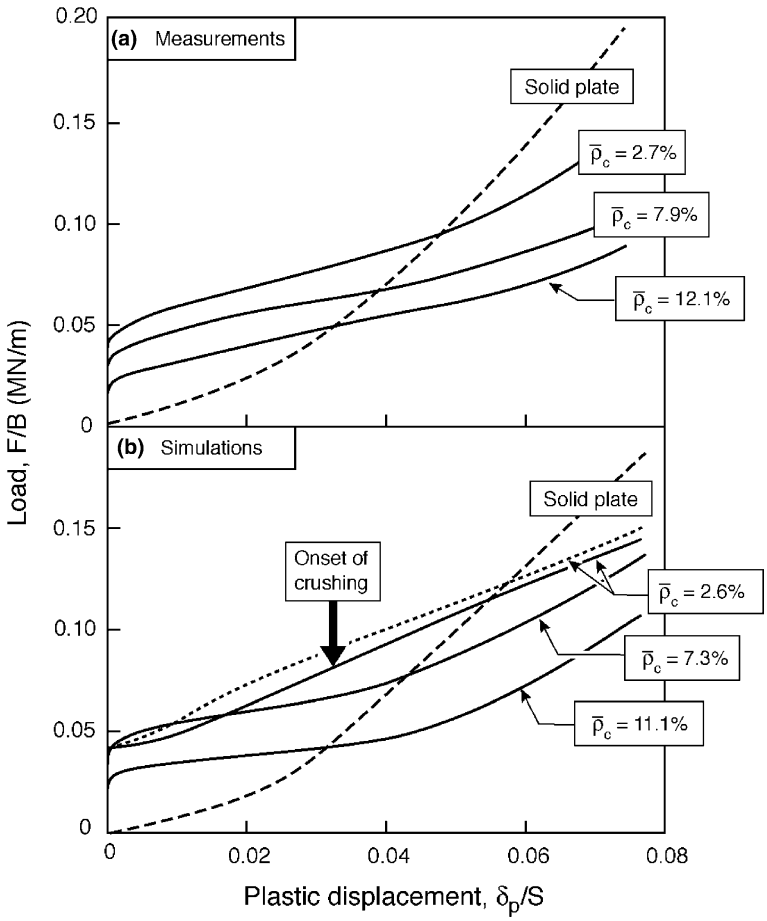

Fig. 15. Mechanical response of sandwich panels in clamped bending configuration. Solid lines in (b) are based on simulations in which the core constitutive law had been calibrated using the *simulated* compressive stress–strain curve; in contrast, the dotted line is based on a calibration from the *measured* compressive response.

To simulate the supports and the loading platen, rigid surfaces are used, with friction coefficient, $\mu = 0.1$. Most calculations have been performed by using the *simulated* core compression response. A few results have been obtained by using the corresponding core compression measurements as input. The calculated load/deflection curves are shown in Figs. 14b and 15b, and the distorted shapes of the clamped bending beams are indicated on Fig. 17. To affirm the mechanism operative at yield, the magnitude of the yield zone has been evaluated for selected tests. An example for the simply-supported bend test performed on the sample with near optimal design is presented on Fig. 18. To assess the onset of core crushing, for some tests, the separation between the face sheets just below the loading platen has been ascertained and plotted as a function of the load (Fig. 19).

Yield zone assessments of the type shown on Fig. 18 confirm that the panels with the larger relative density cores ($\bar{\rho}_c = 7.9\%, 11\%$) deform by plastic deformation of the faces, in both simply supported and clamped bending, with the cores remaining elastic until the displacements become large. Consequently, the calculated loads are insensitive to the constitutive law used for the core and, unsurprisingly, are in good agreement with the measured loads. The situation is different for the near-optimal panel with the lowest core density ($\bar{\rho}_c = 2.6\%$). In these panels (Fig. 18), the initial plastic deformation involves local core shear

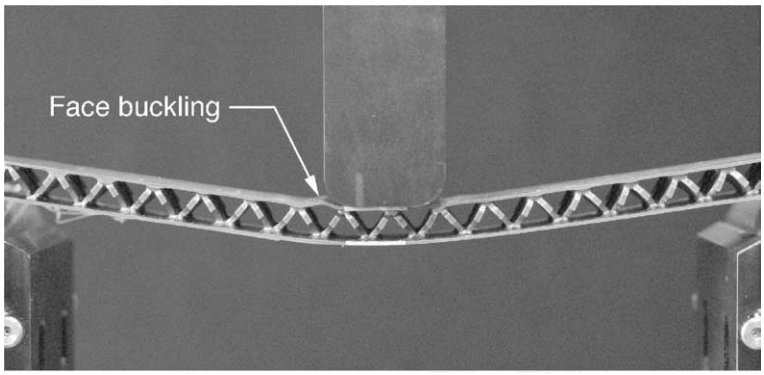

Fig. 16. Face sheet buckling in sandwich panel with $\bar{\rho}_c = 7.9\%$, shortly after the load maximum.

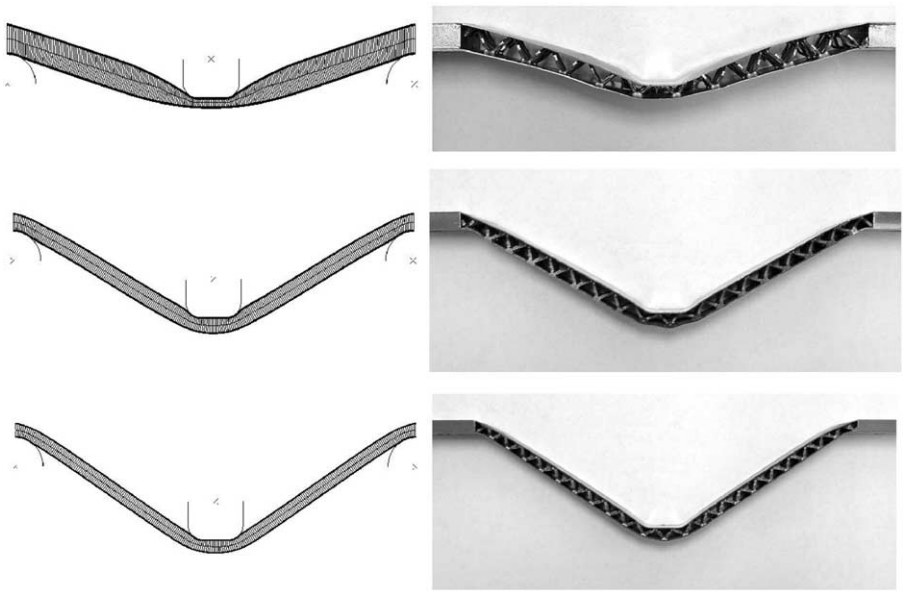

Fig. 17. Comparisons of simulated and observed shape changes of sandwich panels following clamped bending tests. The core densities increase from top to bottom.

beneath the platens, accompanied by a small zone of local yielding of the lower face. The analytical model similarly predicts simultaneous failure by core and face yielding (point A in Fig. 2). Thereafter, the plastic zone in the core spreads throughout the cross section, with minimal additional plastic deformation in the faces. This mode continues throughout the bending phase: that is, until the face stretching regime initiates in the clamped bending tests.

The localization of the plastic deformation to the core causes abrupt yielding in the simulations. Such abruptness does not arise in the measurements. Rather, stable hardening occurs before a peak stress is reached. This abruptness is ameliorated by using the *measured* core compression curve (dotted lines in Figs. 14b and 15b), presumably because of the more pronounced strain hardening. The implication is that, when available, the measured core compression curves should be used as input, rather than the simulated

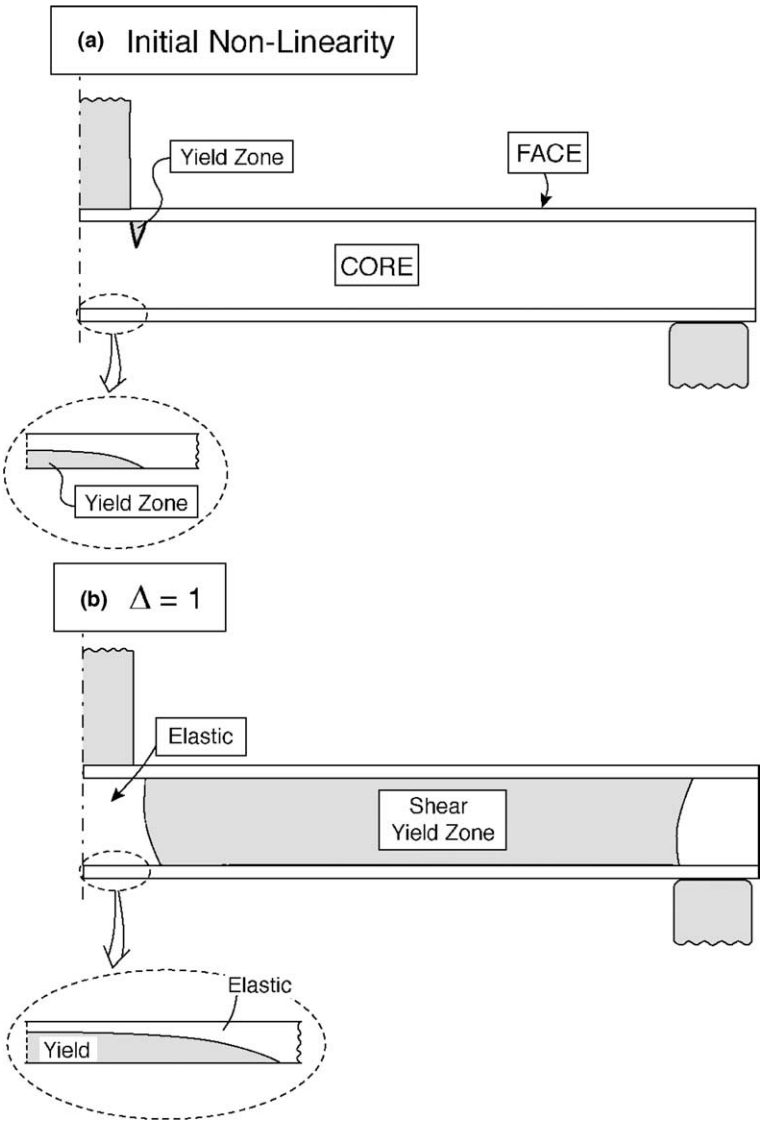

Fig. 18. Onset and spread of plasticity in panel with $\bar{\rho}_c = 2.6\%$, subject to three point bending.

curves. In clamped bending (Fig. 15), the abrupt yielding causes a reversal in the load capacity for the panels with the two lowest $\bar{\rho}_c$. That is, just beyond yield, while the experiments reveal that the panel with lowest $\bar{\rho}_c$ is stronger, the calculations indicate greater strength in the panel with intermediate $\bar{\rho}_c$.

In the clamped bending tests on panels with $\bar{\rho}_c = 2.6\%$, core crushing occurs when the plastic displacement, $\delta_p/S \approx 0.03$, well beyond initial yielding by core shear. Thereafter, the core continues to crush as the load capacity of the beam increases. Such crushing is not predicted for the higher core densities. Similar behaviors are observed experimentally (Fig. 17).

In simply supported bending, the stress peak found experimentally is associated with plastic buckling of the compressed face adjacent to the loading platen (Fig. 16). This response cannot be predicted using the continuum model for the core without incorporating new features.

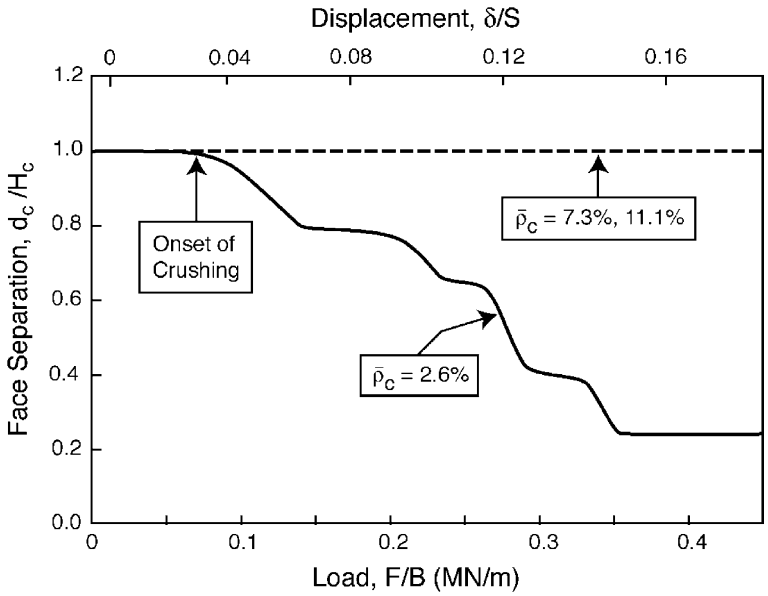

Fig. 19. Core straining during clamped bending tests. Core crushing occurs only in panels with $\bar{\rho}_c = 2.6\%$.

5. Conclusions

A protocol has been proposed for characterizing the structural performance of all-metallic sandwich panels. The merits of the approach have been demonstrated for panels with pyramidal truss cores. It combines measurements, mechanism maps, finite element simulations and optimization. Mechanism maps based on beam theory have been used to characterize face and core dimensions as well as to estimate minimum weight designs. Experimental measurements and finite element calculations are used to calibrate and understand the responses of the core in transverse compression, in-plane shear and stretch. Overlaying the measurements and simulations has revealed consistent discrepancies, attributed to uncertainties in the mechanical properties of the core member material. Notwithstanding this deficiency, the results establish and calibrate an orthotropic constitutive law for the core, which can be used for design calculations.

To assess the fidelity of the constitutive law, bending tests have been performed on panels subject to two end constraints. The tests have been simulated using the stress/strain response of the faces obtained from independent measurements. The comparisons reveal that the loads are predicted quite accurately. However, in panels with core densities close to the optimum, some aspects of the core response are not fully captured in the simulations. In particular, the simulations reveal a softening effect at the onset of core yielding which is not found experimentally. Further assessments of the sensitivity of the response to the input stress/strain relations will address this discrepancy.

Acknowledgements

This work was supported by the ONR MURI program on Blast Resistant Structures through a subcontract from Harvard University to the University of California at Santa Barbara (Contract No. 123163-03).

References

Ashby, M.F., Evans, A.G., Fleck, N.A., Gibson, L.J., Hutchinson, J.W., Wadley, H.N.G., 2000. Metal Foams: A Design Guide. Butterworth Heinemann, Boston.

Budiansky, B., 1999. On the minimum weights of compression structures. International Journal of Solids and Structures 36, 3677–3708.

Cote, F., Deshpande, V.S., Fleck, N.A., Evans, A.G., 2004. The out of plane compressive behavior of metallic honeycombs.. Materials Science and Engineering, in press.

Deshpande, V.S., Fleck, N.A., Ashby, M.F., 2001. Effective properties of the octet-truss lattice material. Journal of the Mechanics and Physics of Solids, 49,1747–1769.

Evans, A.G., Hutchinson, J.W., Fleck, N.A., Ashby, M.F., Wadley, H.N.G., 2001. The topological design of multifunctional cellular metals. Progress in Materials Science 46, 309–327.

Evans, A.G., 2001. Lightweight materials and structures. MRS Bulletin 26, 790.

Hill, R., 1948. A theory of the yielding and plastic flow of anisotropic metals. Proceedings of the Royal Society of London A193, 281–297.

McMeeking, R.M., in press.

Rathbun, H.J., Wei, Z., He, M.Y., Zok, F.W., Evans, A.G., Sypeck, D.J., Wadley, H.N.G., 2004. Measurements and simulations of the performance of metallic sandwich structures with a near optimal tetrahedral truss core. Journal of Applied Mechanics, in press.

Wicks, N., Hutchinson, J.W., 2001. Optimal truss plates. International Journal of Solids Structures 38, 5183–6165.

Xue, Z., Hutchinson, J.W., 2004. Constitutive model for metallic sandwich cores. International Journal for Numerical Methods in Engineering, in press.

Zok, F.W., Rathbun, H.J., Wei, Z., Evans, A.G., 2003. Design of metallic textile core sandwich panels. International Journal of Solids Structures 40, 5707–5722.